



HAL
open science

Experimental Wind Field Estimation and Aircraft Identification

Jean-Philippe Condomines, Murat Bronz, Gautier Hattenberger,
Jean-François Erdelyi

► **To cite this version:**

Jean-Philippe Condomines, Murat Bronz, Gautier Hattenberger, Jean-François Erdelyi. Experimental Wind Field Estimation and Aircraft Identification. IMAV 2015: International Micro Air Vehicles Conference and Flight Competition, Sep 2015, Aachen, Germany. hal-01204624

HAL Id: hal-01204624

<https://enac.hal.science/hal-01204624v1>

Submitted on 24 Sep 2015

HAL is a multi-disciplinary open access archive for the deposit and dissemination of scientific research documents, whether they are published or not. The documents may come from teaching and research institutions in France or abroad, or from public or private research centers.

L'archive ouverte pluridisciplinaire **HAL**, est destinée au dépôt et à la diffusion de documents scientifiques de niveau recherche, publiés ou non, émanant des établissements d'enseignement et de recherche français ou étrangers, des laboratoires publics ou privés.

See discussions, stats, and author profiles for this publication at: <http://www.researchgate.net/publication/282003424>

Experimental Wind Field Estimation and Aircraft Identification

CONFERENCE PAPER · SEPTEMBER 2015

READS

6

4 AUTHORS:



[Jean-Philippe Condomines](#)

Ecole Nationale de l'Aviation Civile

14 PUBLICATIONS 4 CITATIONS

[SEE PROFILE](#)



[Murat Bronz](#)

Ecole Nationale de l'Aviation Civile

13 PUBLICATIONS 8 CITATIONS

[SEE PROFILE](#)



[Gautier Hattenberger](#)

Ecole Nationale de l'Aviation Civile

28 PUBLICATIONS 61 CITATIONS

[SEE PROFILE](#)



[Jean-François Erdelyi](#)

Paul Sabatier University - Toulouse III

1 PUBLICATION 0 CITATIONS

[SEE PROFILE](#)

Experimental Wind Field Estimation and Aircraft Identification

Jean-Philippe Condomines*, Murat Bronz*, Gautier Hattenberger*, Jean-François Erdelyi
ENAC; UAV Lab ; 7 avenue Edouard-Belin, F-31055 Toulouse, France
Université de Toulouse ; ENAC; F-31077 Toulouse, France

ABSTRACT

The presented work is focusing on the wind estimation and airframe identification based on real flight experiments as part of the *SkyScanner* project. The overall objective of this project is to estimate the local wind field in order to study the formation of cumulus-type clouds with a fleet of autonomous mini-UAVs involving many aspects including flight control and energy harvesting. For this purpose, a small UAV has been equipped with airspeed and angle of attack sensors. Flight data are recorded on-board at high speed for post-analyses. An approach based on Unscented Kalman Filter (UKF) is proposed for nonlinear wind estimation. As a first result, wind updraft estimation is highlighted by exploiting recorded flight test data. In addition to this, a motor test bench has been developed in order to establish a model of the propulsion system from wind tunnel experiments. It will be combined with a classical aerodynamic model for airframe identification Preliminary flight results are presented.

1 INTRODUCTION

Small Unmanned Aerial Vehicle (UAV) are now widely used for atmospheric and meteorological researches [1, 2]. They can easily carry compact sensors, but when it comes to more important payloads like particles and aerosols detectors, the remaining available weight can be limited, unless a bigger airframe is chosen. An important parameter for atmospheric studies, but also for long endurance autonomous flights [3], is the observation of the local wind field. Such information can be used for autonomous soaring for instance. The *SkyScanner*¹ project aims at studying and experimenting a fleet of coordinated Mini UAVs which adaptively samples cumulus-type clouds. This is involving many aspects including flight control and energy harvesting. The main tackled challenges are a better understanding of the clouds micro-physics, small airframe optimization, and optimized fleet control.

The presented work, as part of the *SkyScanner* project, is focusing on the wind estimation and airframe identification

based on real flight experiments. For this purpose, a small UAV has been equipped with airspeed and angle of attack sensors. Flight data are recorded on-board at high speed for post-analyses. Several solutions have been used for wind estimation [4, 5, 6] and system identification [7, 8]. The proposed solution will be based on Unscented Kalman Filter (UKF) [9, 10], widely used in its square-root version form [11, 12, 13].

In addition to the flight data, a model of the propulsion system is required in order to evaluate the propulsive power of the plane based on the flight speed and the consumed electrical power directly measured on the battery. A motor test bench have been designed for this purpose, with an automatic recording sequence controlled by a computer.

In the sequel, first section presents the models and the problem formulation. Then, the theoretical basis of the estimation and identification algorithms are presented. The next section details the experimental setup and the instruments embedded on the UAV. To conclude, the final part gathers all the motor test bench and the experimental results obtained from the flights.

2 PROBLEM FORMULATION

2.1 Wind field

Small UAVs are very sensitive to relative high wind gusts because of their size, hence satisfying the real-life demands becomes difficult. In general wind speed is assumed to be a spatially and temporally varying vector field s.t.

$$\mathbf{w}(x, y, z, t) = \begin{pmatrix} w_x^i(x, y, z, t) \\ w_y^i(x, y, z, t) \\ w_z^i(x, y, z, t) \end{pmatrix}$$

where the superscript i denotes components expressed in the inertial frame. A small vehicle flying through this field is influenced by three components of the wind field and gradients of the wind field such that :

$$\frac{d}{dt} \mathbf{w}(x, y, z, t) = \begin{pmatrix} \dot{w}_x^i \\ \dot{w}_y^i \\ \dot{w}_z^i \end{pmatrix} = \begin{pmatrix} \dot{w}_{\zeta \rightarrow x}^i \\ \dot{w}_{\zeta \rightarrow y}^i \\ \dot{w}_{\zeta \rightarrow z}^i \end{pmatrix} + \nabla \mathbf{w}(x, y, z) \begin{pmatrix} \dot{x} \\ \dot{y} \\ \dot{z} \end{pmatrix} \quad (1)$$

where the subscript ζ denotes the time rate of change of wind velocity at the point (x, y, z) . Three component \dot{x} , \dot{y} and \dot{z} represent the velocity of the vehicle with respect to inertial

*firstname.lastname@enac.fr

¹ <http://www.laas.fr/projects/skyscanner>

frame and $\nabla \mathbf{w}(x, y, z)$ is the gradient of the wind field. Assuming a constant wind field as seen by the vehicle, the last term of Eq.1 becomes to zero, however this approximation is only applicable when vehicle velocity is large compared to the “point” rates of change of wind velocity (e.g. wing span is significantly larger than tail height, so vertical gradient of the lateral air mass velocity has negligible effect on roll rate). This paper considers the simultaneous nonlinear state estimation of aircraft body-axis velocity component and wind velocity component in the North-East-Down (NED) inertial reference frame using this assumption.

2.2 Vehicle Dynamics and Kinematics

In order to tackle a wide range of applications, various implementations of flight dynamics models, in terms of assumptions and numerical techniques, therefore exist. To overcome the difficulty for an UAV to derive a reliable representative aerodynamic model, they are commonly represented using a 6 Degrees of Freedom (DoF) kinematic model (3 DoF correspond to the translational motion (V_N, V_E, V_D) and the 3 remaining DoF to the rotational motion (φ, θ, ψ)).

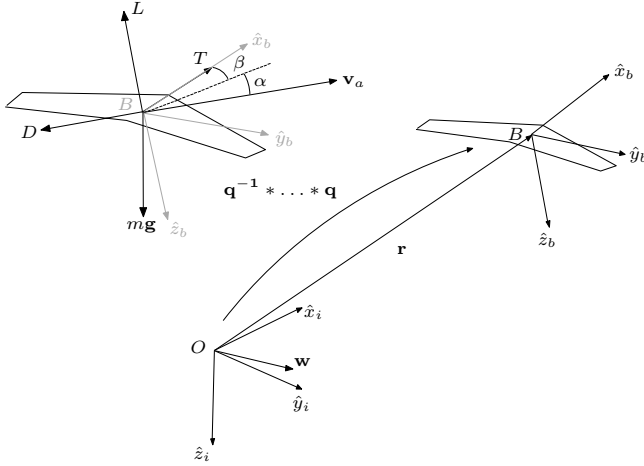


Fig. 1: Reference frames.

Assuming a flat non-rotating Earth the flying rigid body motion in turbulent conditions can be located at \mathbf{r} with velocity \mathbf{v}_i having components V_N, V_E, V_D in an inertial frame I , where \hat{x}_i, \hat{y}_i and \hat{z}_i define unit vector (see figure 1). Using a standard body-fixed coordinate frame with air mass-relative velocity \mathbf{v}_a having components u, v, w in the body $\hat{x}_b, \hat{y}_b, \hat{z}_b$ directions, respectively, the acceleration of the aircraft in the inertial frame can be mathematically described s.t:

$$\dot{\mathbf{r}} = \dot{\mathbf{v}}_i + \dot{\mathbf{w}}$$

Developing inertial velocity

$$\dot{\mathbf{r}} = \frac{d}{dt} \mathbf{v}_a + \boldsymbol{\omega} \times \mathbf{v}_a + \frac{d}{dt} \mathbf{w}$$

Hence

$$\frac{d}{dt} \mathbf{v}_a = \begin{pmatrix} \dot{u} \\ \dot{v} \\ \dot{w} \end{pmatrix} - \boldsymbol{\omega} \times \mathbf{v}_a - \frac{d}{dt} \mathbf{w} \quad (2)$$

Using angular velocity $\boldsymbol{\omega} = (p \ q \ r)^T$ and aerodynamic forces $\mathbf{X}, \mathbf{Y}, \mathbf{Z}$ depending on functions of trust \mathbf{T} , drag \mathbf{D} and lift \mathbf{L} expressed in the body x, y, z directions, the fundamental principle of dynamics now becomes :

$$\begin{pmatrix} \mathbf{X} \\ \mathbf{Y} \\ \mathbf{Z} \end{pmatrix} + \begin{pmatrix} 0 \\ 0 \\ m\mathbf{g} \end{pmatrix} = m \left[\begin{pmatrix} \dot{u} \\ \dot{v} \\ \dot{w} \end{pmatrix} - \begin{pmatrix} 0 & -w & v \\ w & 0 & -u \\ -v & u & 0 \end{pmatrix} \begin{pmatrix} p \\ q \\ r \end{pmatrix} - \begin{pmatrix} \frac{d}{dt} w_{ix} \\ \frac{d}{dt} w_{iy} \\ \frac{d}{dt} w_{iz} \end{pmatrix} \right] \quad (3)$$

In Eq.3, the latter quantity $\frac{d}{dt} \mathbf{w}$ is expressed in the inertial frame and can be converted in the body frame through a Direction Cosine Matrix (DCM) \mathbf{R}_i^a which is defined by successive rotation of the roll, pitch and yaw angles of the aircraft s.t :

$$\mathbf{R}_i^a = (\mathbf{R}_a^i)^T = \begin{pmatrix} c\theta c\psi & c\theta s\psi & -s\theta \\ s\phi s\theta c\psi - c\phi s\psi & s\phi s\theta s\psi + c\phi c\psi & s\phi c\theta \\ c\phi s\theta c\psi + s\phi s\psi & c\phi s\theta s\psi - s\phi c\psi & c\phi c\theta \end{pmatrix}$$

In the next sections, Galilean transformations will be made by using a standard quaternionial form, i.e. $\mathbf{R}_i^a \cdot \mathbf{r} = q^{-1} * \mathbf{r} * q$, $\mathbf{R}_a^i \cdot \mathbf{r} = q * \mathbf{r} * q^{-1}$. Note that symbol $*$ corresponds to the quaternion product. Using the aforementioned standard quaternionial form provides at the same time :

- a global parametrization;
- avoids the mathematical singularities inherent to Euler angles;
- and is convenient for calculations and simulations.

For more details about formulas used on quaternion in this paper, see Appendix A. Finally, the state dynamics for the body-axis velocity states are given by

$$\begin{aligned} \dot{u} = \frac{\mathbf{X}}{m} - g \sin \theta - qw + rv - \dot{w}_{ix} \cos \theta \cos \psi \\ - \dot{w}_{iy} \cos \theta \sin \psi + \dot{w}_{iz} \sin \theta \end{aligned}$$

$$\begin{aligned}\dot{v} &= \frac{\mathbf{Y}}{m} - g \sin \varphi \cos \theta + pw - ru \\ &\quad - \dot{w}_{ix}(\sin \varphi \sin \theta \cos \psi - \cos \varphi \sin \psi) \\ &\quad - \dot{w}_{iy}(\sin \varphi \sin \theta \sin \psi + \cos \varphi \cos \psi) \\ &\quad - \dot{w}_{iz} \sin \varphi \cos \theta\end{aligned}$$

$$\begin{aligned}\dot{w} &= \frac{\mathbf{Z}}{m} - g \cos \varphi \cos \theta + qu - pv \\ &\quad - \dot{w}_{ix}(\cos \varphi \sin \theta \cos \psi + \sin \varphi \sin \psi) \\ &\quad - \dot{w}_{iy}(\cos \varphi \sin \theta \sin \psi - \sin \varphi \cos \psi) \\ &\quad - \dot{w}_{iz} \cos \varphi \cos \theta\end{aligned}$$

with $\dot{w}_{i(\cdot)}$ denotes the rate of change of a component of the wind velocity expressed in the inertial frame.

2.3 Aerodynamic and propulsion

Aerodynamic lift and drag forces in stability axes can be written as follow:

$$\mathbf{L} = \frac{1}{2} \cdot \rho \cdot V_a^2 \cdot S_{\text{ref}} C_L \quad (4)$$

$$\mathbf{D} = \frac{1}{2} \cdot \rho \cdot V_a^2 \cdot S_{\text{ref}} C_D \quad (5)$$

with,

$$\begin{cases} C_L &= C_{L0} + C_{L\alpha} \cdot \alpha + C_{L\beta} \cdot \beta + \frac{1}{2V_a} \begin{pmatrix} bC_{Lp} \\ \bar{c}C_{Lq} \\ bC_{Lr} \end{pmatrix} \cdot \begin{pmatrix} p \\ q \\ r \end{pmatrix} \\ &+ \sum_{\text{sfc}} C_{L\text{sfc}} \cdot \delta_{\text{sfc}} \\ C_D &= C_{D0} + C_{Dk} \cdot C_L^2 + \sum_{\text{sfc}} C_{D\text{sfc}} \cdot \delta_{\text{sfc}} \end{cases} \quad (6)$$

where α is the angle of attack, β the side-slip angle and δ_{sfc} the elevator deflection. Since we are mostly interested in steady flight conditions, close to straight line without side-slip, and that the effect of the elevator on lift and drag forces is small, the equations can be reduced for performance analysis to:

$$\mathbf{L} = \frac{1}{2} \cdot \rho \cdot V_a^2 \cdot S_{\text{ref}} (C_{L0} + C_{L\alpha} \cdot \alpha) \quad (7)$$

$$\mathbf{D} = \frac{1}{2} \cdot \rho \cdot V_a^2 \cdot S_{\text{ref}} (C_{D0} + C_{Dk} \cdot C_L^2) \quad (8)$$

In steady level flight, the weight is equilibrated by the lift, and the drag by the thrust. As a first approximation, the thrust, or more precisely the propulsive power \mathbf{P} (the product of the thrust \mathbf{T} by the airspeed V_a) can be expressed as:

$$\mathbf{P} = \eta \cdot P_{\text{elec}} \quad (9)$$

where, P_{elec} is the electrical power drawn from the batteries and η is an efficiency coefficient, function of the advance ratio, the propeller and motor characteristics, the Reynolds number and the electrical efficiency of the global propulsive system.

A more complex propulsion model [14], with a first order DC motor model, might be used in later studies in order to define an analytic description of η .

3 WIND FIELD ESTIMATION AND AIRCRAFT MODEL IDENTIFICATION

3.1 Wind field estimation

This problem considers simultaneous estimation of aircraft body-axis velocity (u, v, w) and wind velocity components (w_{ix}, w_{iy}, w_{iz}) . Both process and measurement equations are not dependent on aerodynamic force described above. The estimation is performed through a fusion algorithm of low-cost inertial sensors used for UAV navigation [12]. The navigation quality is limited by inertial sensors performance specifies by the size, power and cost constraints of the UAV. To recover navigation accuracy using low-cost aided-INS (Inertial Navigation System), it is necessary to use, if possible, additional instruments (e.g. magnetometers, barometer, which are used to improve the heading and position accuracies) and/or nonlinear estimation algorithms to improve the flight handling qualities of the aerial vehicle. The nonlinear state estimation makes use of 2 triaxial sensors plus both GPS and Pitot tube sensor units which deliver a total of 10 scalar measurement signals:

- 3 gyroscopes providing a measurement of the instantaneous angular velocity vector denoted by $\boldsymbol{\omega}_m \in \mathbb{R}^3$ s.t. $\boldsymbol{\omega}_m = [p_m, q_m, r_m]^T$;
- 3 accelerometers giving a measurement of the specific acceleration denoted by $\mathbf{a}_m \in \mathbb{R}^3$ s.t. $\mathbf{a}_m = [a_{mx}, a_{my}, a_{mz}]^T$;
- 1 GPS unit measuring both position (not used) and velocity vectors denoted by $\mathbf{v}_V = \mathbf{v}_i \in \mathbb{R}^3$ s.t. vector $\mathbf{v}_i = [V_N, V_E, V_D]^T$ is used in the observation equations;
- 1 pitot tube sensor providing a scalar measurement of the air data denoted by y_{Va} .

All the sensors embedded are low-cost, and therefore have imperfections. The major error sources in the navigation system are due to: - all of the disturbances (noises) that affect all the instruments; - the potential incorrect navigation system initialization (e.g. on magnetometers or barometric sensor); - and the inadequacy between the real local Earth's gravity value and the one used for computation. The largest error is usually a bias instability (expressed respectively in deg/hr for gyros and μg for the accelerometers).

All these measurements are obviously corrupted by additive noises for which it appears reasonable to assimilate their stochastic properties to the ones of Gaussian processes. Their covariances have been identified in [15] from logged sensor data using the Allan variance method [16]. Moreover, these errors correspond to the random nature of wind evolution necessary in Eq.2.

Using these values, the state space representation corresponding to \mathcal{M}_s can be described in a compact form such as:

$$\dot{x} = f(x, u) \quad \text{and} \quad y = h(x, u)$$

where: $x = [u, v, w, w_{ix}, w_{iy}, w_{iz}]^T$, $u = [\omega_m^T, \mathbf{a}_m^T]^T$ and $y = [y_V^T, y_{Va}]^T$ are the state, input and output vectors respectively.

$$\mathcal{M}_s \begin{cases} \begin{cases} \dot{u} = a_{mx} - g \sin \theta + r_m \cdot v - q_m \cdot w \\ \dot{v} = a_{my} + g \cos \theta \sin \phi + p_m \cdot w - r_m \cdot u \\ \dot{w} = a_{mz} + g \cos \theta \sin \phi + q_m \cdot u - p_m \cdot v \\ \dot{w}_{ix} = 0 \\ \dot{w}_{iy} = 0 \\ \dot{w}_{iz} = 0 \end{cases} & \text{(process)} \\ \begin{cases} \begin{pmatrix} y_{VN} \\ y_{VE} \\ y_{VD} \end{pmatrix} = q * \begin{pmatrix} u \\ v \\ w \end{pmatrix} * q^{-1} \\ y_{Va} = \left\| \begin{pmatrix} u \\ v \\ w \end{pmatrix} - q^{-1} * \begin{pmatrix} w_{ix} \\ w_{iy} \\ w_{iz} \end{pmatrix} * q \right\| \end{cases} & \text{(measurement)} \end{cases}$$

Obviously, to implement these equation in a discrete-time filter, a first order discretization is used [17].

$$\begin{cases} x_k = x_{k-1} + T_s \cdot f_c(x_{k-1}, u_{k-1}) + v_k \\ y_k = h(x_k) + \mu_k \end{cases}$$

where f is the discrete-time state transition, h is the nonlinear observation function which depend on DCM through quaternion and T_s is the sampling time of the system. v, μ are the zero-mean Gaussian process noise vectors with covariance matrix, Q, R . Using these relationships, the angle of attack and side-slip are calculated from the body axis velocity components by

$$\alpha = \tan^{-1} \left(\frac{w}{u} \right)$$

$$\beta = \sin^{-1} \left(\frac{v}{\sqrt{u^2 + v^2 + w^2}} \right)$$

Since the measurement equation formulation contains nonlinear function, a nonlinear state estimation technique such as EKF [18] or UKF is required. The SR-UKF (Square-Root UKF) was selected for this work due to its ease of implementation and outperforms relative to EKF. Identification of both

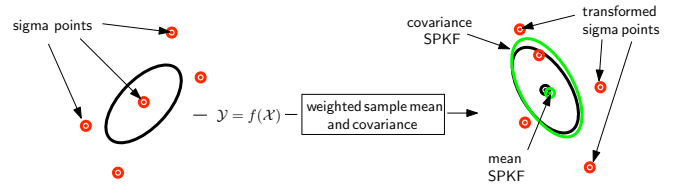


Fig. 2: Sigma point approach.

aerodynamic coefficient C_L and C_D can be lead by changing the process equation which is ongoing work.

This study uses flight data collected with a small UAV which is susceptible to perform some trajectories which leads to reduce maneuverability and so unobservability on two components of wind speed. Wind speed unobservability points out a particular behavior of UKF which is shown by a slow drift on state vector due to using sigmas-points for prediction and correction steps. Indeed, in case of strong nonlinearity, predictions are obtained by weighting the sigma-point predictions whose results differs from the direct calculation of the prediction from the estimated state (see figure 2). Firstly, effects can be observed in the calculation of the predicted state where the successive accumulation of these differences can lead to significant drifts, and secondly, in the correction of the state from the prediction measure. These effects can be eliminated by performing the calculation of prediction of the state and measures from the estimated average state, while retaining the sigma points for the calculation of covariance.

3.2 Aircraft model identification

The aircraft model identification is using the equation from section 2.3 during steady flight phases, when the airspeed is almost constant, thus the acceleration is zero. As a results, lift equals weight and thrust equals drag. Since the propulsion model was still under investigation at the time of the first flight experiments, the methodology have been adapted in order to estimate the drag. The procedure described in [19] have been used. It consists of performing several gliding phases at different airspeed and angle of attack in order to estimate the drag from the glide flight path γ :

$$\tan \gamma = -\frac{\mathbf{D}}{\mathbf{L}} = -\frac{C_D}{C_L} \quad (10)$$

The identification of the lift coefficient is done using Eq. 7. For each flight phase, the airspeed V_a and the angle of attack α are averaged. Then a linear regression is used to estimate the two parameters C_{L0} and $C_{L\alpha}$.

In order to identify the drag coefficient, only the gliding phases are considered as stated above and equations 8 and 10 are used. Three parameters are then needed, the lift coefficient and the angle of attack that are already computed, and the flight path angle γ . Since this angle can't be directly measured, two methods have been evaluated. The first method is using an angle of attack installed on the UAV and the pitch

angle θ estimated using the IMU sensor. With the kinematic relation $\theta = \alpha + \gamma$, the path angle is estimated by averaging over the complete phase. The second method is using the relation that the lift over drag ratio is also the ratio between the horizontal distance and altitude lost during a glide. The main constraint is that the experiment needs to be done with almost no wind so that the ground and aerodynamic flight paths are the same. After estimating the parameter γ , the drag coefficient is computed with Eq. 10, and second order polynomial regression is done between C_D and α in order to estimate C_{D0} , C_{Dk} .

Experimental results are presented in section 5.1 and they are showing a good correlation between the two methods.

For a futur work, the UKF estimation algorithm presented at the previous section will be applied for these parameters identification.

4 EXPERIMENTAL SETUP

4.1 UAV instrumentation

As mention above, a mini UAV has been equipped with several sensors in order to make in-flight measurements. The frame itself is a commercial foam plane *Solius* from *Multiplex*², a 2.16 meter wingspan motorized glider. The autopilot is an *Apogee*³ board using the *Paparazzi* system [20, 21], which includes a SD card slot for high speed logging.

It would have been possible to connect all the required sensors to the main autopilot, but due to electrical problems with long cables, it has been decided to split the Data Acquisition System (referred as DAQ board) from the flight control (referred as AP board). Hence, a second *Apogee* board was used to record the sensors, which is possible since there is no feedback of the wind estimation to the flight control at this stage of the project. The DAQ board is already equipped with 3-axis gyroscopes and accelerometers, and a low resolution barometer. The INS filter [13] used to estimate the position and orientation of the plane also requires a magnetometer and a GPS, that have been externally mounted.

The *SkyScanner* project aims at studying the formation of clouds. The meteorological parameters will be measured using a dedicated board *Meteo-Stick*. This board has high resolution absolute pressure sensor, differential pressure sensor, temperature sensor and humidity sensor. For this study, only the differential pressure sensor was used connected to a Pitot tube in order to measure the airspeed of the plane.

The figure 3 is showing the final integration of the measurement system, with the DAQ and *Meteo-Stick* stacked, the GPS and the magnetometer at the back.

The main sensor addition is an angle of attack sensor, mounted on the wing close to the Pitot tube. This sensor is made of a US DIGITAL MA3-P12-125-B⁴ angular sensor. It is an absolute position sensor using hall effect with 12-bit

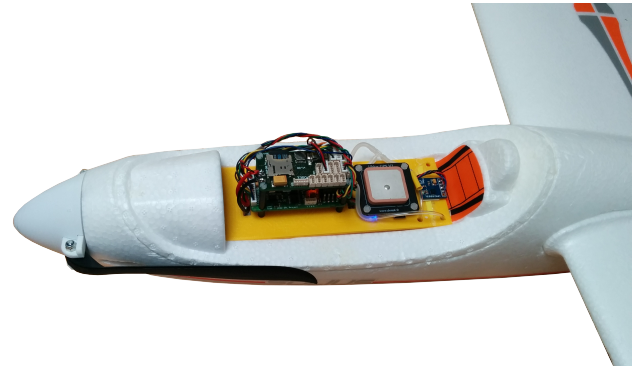


Fig. 3: Integration of the data acquisition system in the nose of the UAV.

internal converter giving less than 0.09° of resolution with a very low noise. The vane has been 3D-printed and mounted directly on the shaft of the sensor. The figure 4 shows the final integration of this two sensors on the wing. The piece holding them has also been made with a 3D printer.



Fig. 4: Integration of the Pitot tube and the angle of attack sensor on the leading edge of the wing.

The final setup for the *SkyScanner* project will also include a current sensor in order to measure the electrical power drawn by the motor that will be used in the aerodynamic and propulsion models, and some additional scientific sensors dedicated to the atmospheric research part, such as Liquid Water Content sensors, not directly related to the wind estimation.

4.2 Motor test bench

In order to integrate the propulsion model to the estimation process, it is necessary to establish the relation between the electrical current consumed by the motor, the rotation speed, the flight speed and the resulting propulsion forces and torque generated. Since it is not possible to embed the necessary sensors to estimate this late parameters in flight, a motor test bench provides the propulsion model based on wind tunnel experiments.

The figure 5 shows the bench. Two force sensors are used to measure the propulsive force and the motor torque. The bench itself is an assembly of 3D-printed pieces and aluminum bars.

² <http://www.multiplex-rc.de>

³ <http://wiki.paparazziuav.org/wiki/Apogee/v1.00>

⁴ <http://www.usdigital.com/products/encoders/absolute/rotary/shaft/ma3>

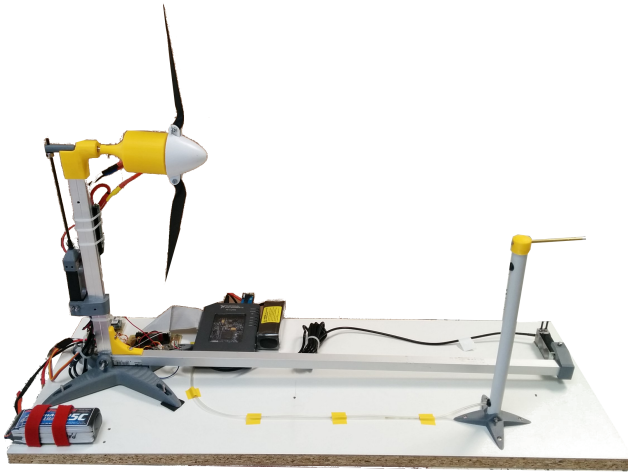


Fig. 5: Final version of motor test bench.

In addition to the mechanical mounting of the motor and its propeller, an electronic board is required for the sensors' signal conditioning. Finally, a *myRIO* data acquisition board from *National Instruments* connects them to the lab computer. A graphical interface developed using *LabView* allows to control the motor PWM command and synchronize all the measurements, making the process almost fully automated (the wind tunnel speed is currently control by hand). The figure 6 presents the global architecture and wiring of the motor test bench.

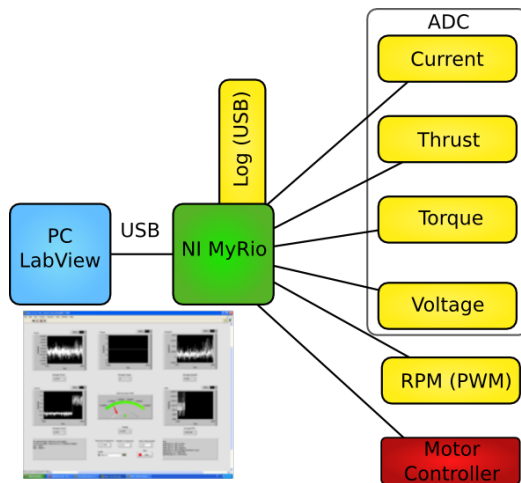


Fig. 6: Overview of the motor test bench experimental setup.

5 EXPERIMENTAL RESULTS

5.1 Flight tests

A few flight tests using the experimental setup described in the previous section have already been conducted (see figure 7).

ure 7).



Fig. 7: *Solius* glider fully equipped for experimental flight.

Some preliminary results have been analyzed in order to assess the quality of the measurements, especially the angle of attack sensor since the *Meteo-Sick* sensors have already been validated in a previous project. The figure 8 shows the good correlation between the variation of the airspeed and the angle of attack (one increasing when the other decrease). Note that this study uses angle of attack data collected with a constant offset which can be removed from raw data.

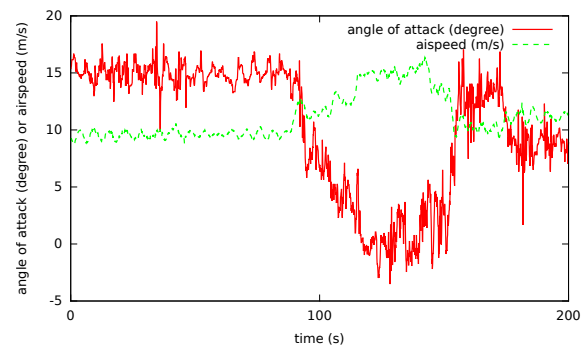


Fig. 8: Comparison of the angle of attack (red, plain line) and the airspeed (green, dashed line).

Flight plans In order to perform a correct estimation of the wind or the aerodynamic model, it is necessary to perform appropriate flight patterns. Concerning the wind estimation, observability is achieved by changing the flight direction. Hence, the chosen flight patterns are circles or small variation along a given segment. Figure 9 shows the horizontal wind field estimation along the aircraft trajectory. Further flight data analysis will be conducted in order to correctly tune the algorithm. The extraction of the vertical component of the wind will be possible by including the angle of attack measurements and not only the airspeed norm as it is currently the case.

Another type of flight pattern has been used in order to estimate the lift and drag coefficients as a function of the angle of attack. Several gliding phases are done at different

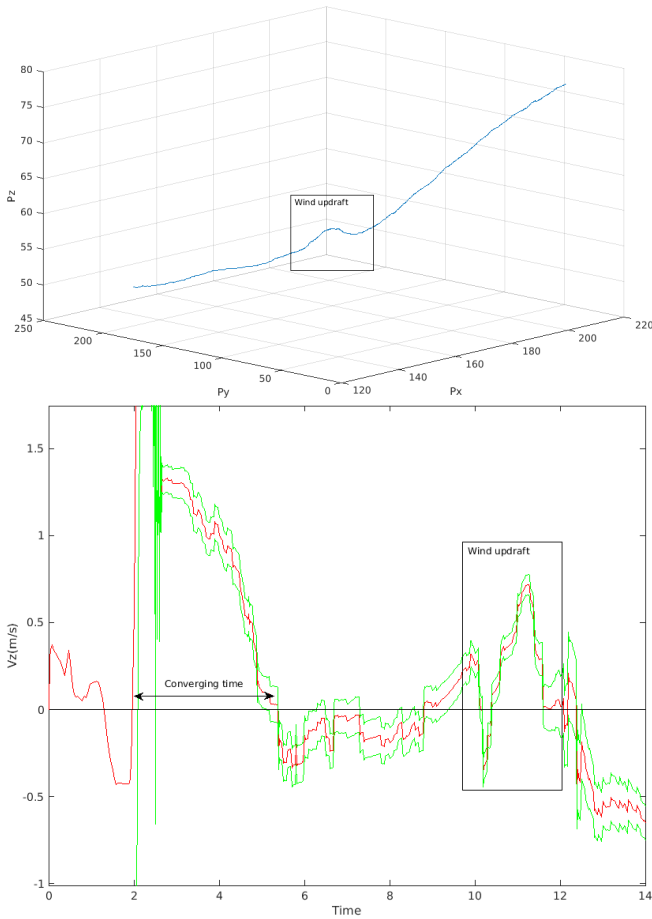


Fig. 9: Estimation of a wind updraft (red) during a gliding phase with confidence bounds (green).

airspeed following the same protocol than [19]. The figure 10 is showing four of these flight phases extracted from the complete experimental flight.

From the complete flight, four gliding phases and three cruise level flight phases have been selected for their stable airspeed and away from stall point. The figure 11 is a plot of the lift coefficient C_L over the angle of attack α , using both cruise and gliding phases. Figure 12 shows the drag coefficient C_D over α computed with the two methods as described section 3.2. Both methods are giving very similar results, which is validating the identification methodology.

The table 1 summarizes the estimated aerodynamic coefficients (with α in degree):

5.2 Motors analysis

The motor test bench have been placed in a wind tunnel and the parameters have been recorded at different airspeed from 0 (static thrust) up to 22 m/s. The resulting thrust versus RPM is shown on figure 13. We can see that the motor is generating a fair amount of static thrust (up to 10 N for a 1.5 kg plane) allowing easy take-off. But at higher speed,

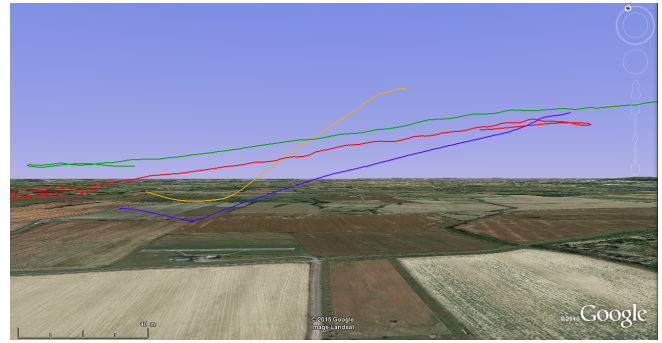


Fig. 10: Different gliding flight path.

C_{L0}	$C_{L\alpha}$
0.2831	0.04119

	C_{D0}	C_{Dk}
method 1	0.01848	0.2034
method 2	0.01839	0.1912

Tab. 1: Aerodynamic coefficients identification for lift and drag.

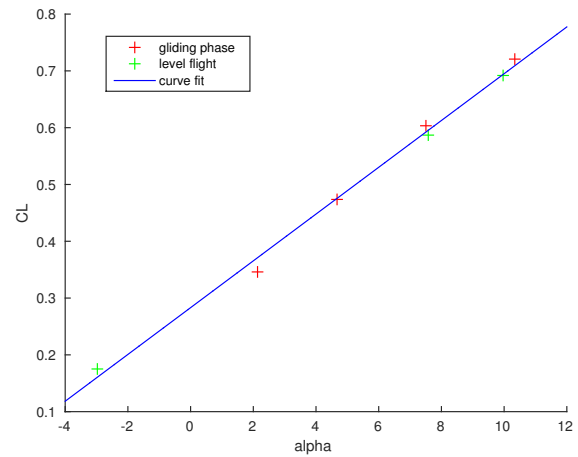


Fig. 11: Lift coefficient versus angle of attack.

the motor is not generating positive thrust at low RPM (at 22 m/s it needs at least 80% of throttle) since the glider was not originally designed for high speed.

The main interest for improving the wind estimation and aircraft identification is to find a simple relation between the propulsive power and a measurable parameter. The figure 14 is showing this propulsive power versus the electrical power drawn from the battery. This later value can be measured on-board from voltage and current sensors. As we can see, for the useful flight speeds from 10 to 15 m/s, there is a simple linear dependency of these two parameters.

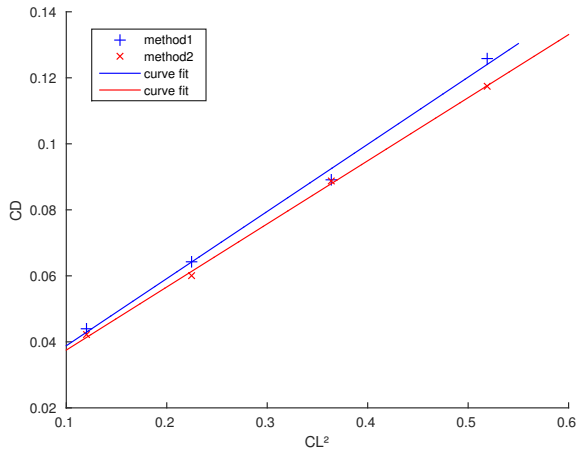


Fig. 12: Drag coefficient versus squared lift coefficient, estimated with two different methods.

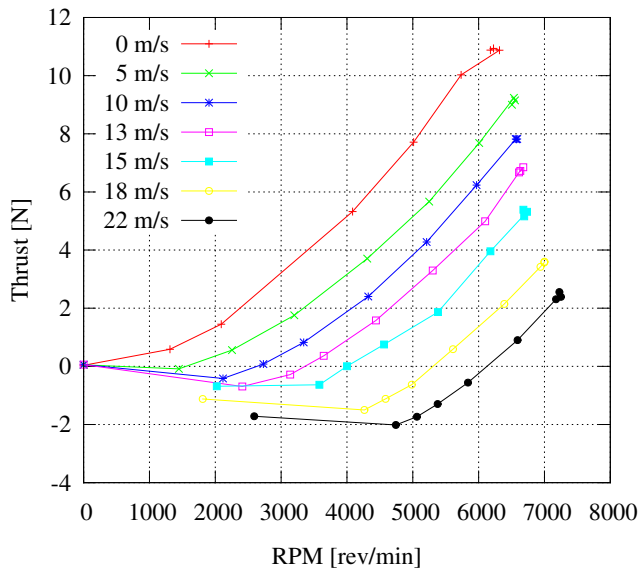


Fig. 13: Thrust versus RPM at different airspeed from wind tunnel experiment.

6 CONCLUSION

This article has presented the theoretical basis of a wind estimation algorithm based on Unscented Kalman Filter. Experimental flights have already been conducted in order to get real data. A foam glider have been equipped with air-speed and angle of attack sensors in addition to the traditional GPS+IMU units needed for the autonomous flight. The propulsion model have been identified using a motor test bench in a wind tunnel. Further developments will integrate this model to the aircraft aerodynamic identification process and to the wind estimation.

This work is only a first step in a larger project aiming

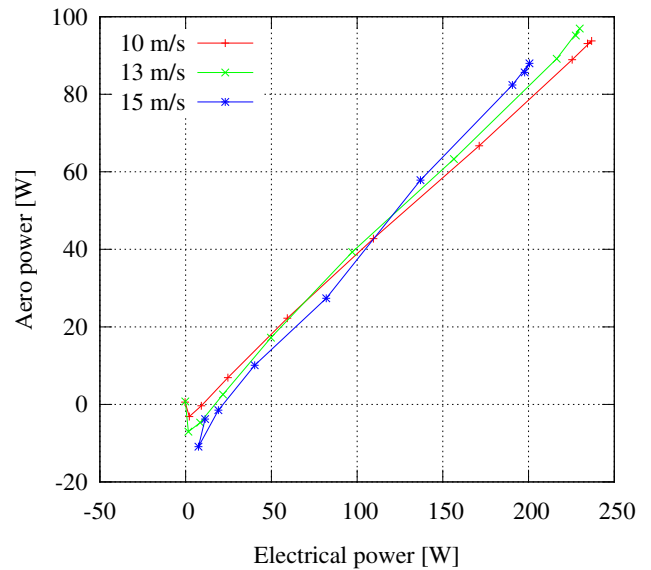


Fig. 14: Propulsive power versus electrical power input for useful flight speeds.

at conducting atmospheric research using a fleet of cooperative UAVs. The estimation of the local wind field is therefore an important part of the project, but can be reused in many other applications such as long endurance flights based on autonomous soaring.

ACKNOWLEDGEMENTS

The *SkyScanner* project is founded by the RTRA-STAE foundation.

REFERENCES

- [1] Stéphanie Mayer, Gautier Hattenberger, Pascal Brisset, Marius Jonassen, and Joachim Reuder. A "no-flow-sensor" wind estimation algorithm for unmanned aerial systems. *International Journal of Micro Air Vehicles*, 4(1):pp 15–30, March 2012.
- [2] Kevin Rogers, Feng Rice, and Anthony Finn. Uav-based atmospheric tomography using large eddy simulation data. In *Intelligent Sensors, Sensor Networks and Information Processing (ISSNIP), 2015 IEEE Tenth International Conference on*, pages 1–6, April 2015.
- [3] J.A. Cobano, D. Alejo, S. Sukkarieh, G. Heredia, and A. Ollero. Thermal detection and generation of collision-free trajectories for cooperative soaring uavs. In *Intelligent Robots and Systems (IROS), 2013 IEEE/RSJ International Conference on*, pages 2948–2954, Nov 2013.
- [4] T. Larrabee, Haiyang Chao, M. Rhudy, Yu Gu, and M.R. Napolitano. Wind field estimation in uav formation

- flight. In *American Control Conference (ACC), 2014*, pages 5408–5413, June 2014.
- [5] Am Cho, Jihoon Kim, Sanghyo Lee, and Changdon Kee. Wind estimation and airspeed calibration using a uav with a single-antenna gps receiver and pitot tube. *Aerospace and Electronic Systems, IEEE Transactions on*, 47(1):109–117, January 2011.
- [6] Am Cho, Jihoon Kim, Sanghyo Lee, and Changdon Kee. Wind Estimation and Airspeed Calibration using a UAV with a Single-Antenna GPS Receiver and Pitot Tube. *IEEE Transactions on Aerospace and Electronic Systems*, 47(1):109–117, January 2011.
- [7] Li Meng, Liu Li, and S.M. Veres. Aerodynamic parameter estimation of an unmanned aerial vehicle based on extended kalman filter and its higher order approach. In *Advanced Computer Control (ICACC), 2010 2nd International Conference on*, volume 5, pages 526–531, March 2010.
- [8] P. Hemakumara and S. Sukkarieh. Non-parametric uav system identification with dependent gaussian processes. In *Robotics and Automation (ICRA), 2011 IEEE International Conference on*, pages 4435–4441, May 2011.
- [9] Simon J. Julier and Jeffrey K. Uhlmann. New extension of the Kalman filter to nonlinear systems. In *SPIE 3068, Signal Processing, Sensor Fusion, and Target Recognition*, volume 3068, pages 182–193, 1997.
- [10] S. Sarkka. On Unscented Kalman Filtering for State Estimation of Continuous-Time Nonlinear Systems. *IEEE Transactions on Automatic Control*, 52(9):1631–1641, September 2007.
- [11] E. Wan R. van der Merwe. The square-root unscented kalman filter for state and parameter-estimation. *Proc. of the IEEE International Conf. on Acoustics, Speech, and Signal Processing*, pages 3461–3464, 2001.
- [12] Jean-Philippe Condomines, Cédric Seren, Gautier Hattenberger, et al. Nonlinear state estimation using an invariant unscented kalman filter. *AIAA Guidance Navigation and Control Conference*, pages 1–15, 2013.
- [13] J.-P. Condomines, C. Seren, and G. Hattenberger. Pi-Invariant Unscented Kalman Filter for sensor fusion. In *2014 IEEE 53rd Annual Conference on Decision and Control (CDC)*, pages 1035–1040, December 2014.
- [14] Mark Drela. First-order dc electric motor model. Technical report, MIT, Aero and Astro, February 2007.
- [15] Bronz Murat, Condomines Jean-Philippe, and Hattenberger Gautier. Development of an 18cm Micro Air Vehicle : QUARK. September 2013.
- [16] N. El-Sheimy, Haiying Hou, and Xiaoji Niu. Analysis and Modeling of Inertial Sensors Using Allan Variance. *IEEE Transactions on Instrumentation and Measurement*, 57(1):140–149, January 2008.
- [17] Frank L. Lewis and Vassilis L. Syrmos. *Optimal Control*. John Wiley & Sons, November 1995.
- [18] R. E. Kalman and R. S. Bucy. New Results in Linear Filtering and Prediction Theory. *Journal of Fluids Engineering*, 83(1):95–108, March 1961.
- [19] Dan Edwards. Performance testing of rnr’s sbxc using a piccolo autopilotd. Technical report, 2007.
- [20] Pascal Brisset, Antoine Drouin, Michel Gorraz, Pierre-Selim Huard, and Jeremy Tyler. The paparazzi solution. *MAV2006, Sandestin, Florida*, 2006.
- [21] Gautier Hattenberger, Murat Bronz, and Michel Gorraz. Using the Paparazzi UAV System for Scientific Research. In *IMAV 2014, International Micro Air Vehicle Conference and Competition 2014*, pages pp 247–252, Delft, Netherlands, August 2014.

APPENDIX A: QUATERNIONS AND ROTATIONS

An unit quaternion provide a convenient mathematical notation and a global parametrization for representing orientation and rotation of a rigid body in three dimensions. Indeed, for any unit quaternion

$$q = q_0 + \mathbf{q} = \cos \frac{\theta}{2} + \mathbf{u} \sin \frac{\theta}{2}$$

and for any vector $\mathbf{p} \in \mathbb{R}^3$ the action of the operator

$$q^{-1} * \mathbf{p} * q = R_q \cdot \mathbf{p}$$

is associated to a rotation matrix $R_q \in SO(3)$ which is a rotation of the coordinate frame about axis $\mathbf{u} = \frac{\mathbf{q}}{\|\mathbf{q}\|}$ through an angle θ .

Note that a vector $\mathbf{p} \in \mathbb{R}^3$ can be viewed as a pure quaternion whose real part is zero $\begin{pmatrix} 0 \\ \mathbf{p} \end{pmatrix}$. Thus, when the real part is a scalar denoted $p_0 \in \mathbb{R}$ the quaternion p is given as :

$$p = \begin{pmatrix} p_0 \\ \mathbf{p} \end{pmatrix}$$